

# Janus-Structured Microgel Barrier with Tissue Adhesive and Hemostatic Characteristics for Efficient Prevention of Postoperative Adhesion

Zichuan Ding, Zhimin Liang, Xiao Rong, Xiaoxue Fu, Jiaxuan Fan, Yahao Lai, Yongrui Cai, Chao Huang, Lingli Li, Guosheng Tang,\* Zeyu Luo,\* and Zongke Zhou\*

Postoperative adhesion (POA) is a common and serious complication following various types of surgery. Current physical barriers either have a short residence time at the surgical site with a low tissue attachment capacity or are prone to undesired adhesion formation owing to the double-sided adhesive property, which limits the POA prevention efficacy of the barriers. In this study, Janus-structured microgels (Janus-MGs) with asymmetric tissue adhesion capabilities are fabricated using a novel bio-friendly gas-shearing microfluidic platform. The anti-adhesive side of Janus-MGs, which consists of alginate, hyaluronic acid, and derivatives, endows the material with separation, lubrication, and adhesion prevention properties. The adhesive side provided Janus-MGs with tissue attachment and retention capability through catechol-based adhesion, thereby enhancing the in situ adhesion prevention effect. In addition, Janus-MGs significantly reduced blood loss and shortened the hemostatic time in rats, further reducing adhesion formation. Three commonly used rat POA models with different tissue structures and motion patterns are established in this study, namely peritoneal adhesion, intrauterine adhesion, and peritendinous adhesion models, and the results showed that Janus-MGs effectively prevented the occurrence of POA in all the models. The fabrication of Janus-MGs offers a reliable strategy and a promising paradigm for preventing POA following diverse surgical procedures.

tissue that should normally be separate. It is a common and serious complication following various types of surgery.<sup>[1,2]</sup> It typically involves soft tissues such as the peritoneum, uterine cavity, and tendon<sup>[3–5]</sup> and can lead to inherent functional abnormalities of organs, resulting in a series of related severe complications. In addition to postoperative chronic pain caused by excessive friction, POA can also lead to serious complications such as intestinal obstruction, infertility, limb disabilities, and even life-threatening situations, causing immense suffering to patients, posing challenges to clinicians, and imposing a significant economic burden on society.<sup>[3–5]</sup> Bleeding caused by surgical trauma is a significant factor that leads to POA, with the formation of blood clots and insoluble fibrin deposition after coagulation serving as the cornerstones of fibrous adhesion formation.<sup>[6,7]</sup> Because surgical adhesiolysis requires reoperation and has the risk of adhesion recurrence, the use of biomaterials as physical barriers for preventing POA is currently considered the most effective and widely used approach.<sup>[8]</sup>

Various physical barriers made from natural polymers, such as hyaluronic acid, alginate, chitosan, and their derivatives, have been used to prevent contact, interconnection, and friction between surgical tissues and adjacent tissues through separation,

## 1. Introduction

Postoperative adhesion (POA) refers to an abnormal fibrous connection forming between the surgical site and the surrounding

Z. Ding, X. Fu, J. Fan, Y. Lai, Y. Cai, C. Huang, Z. Luo, Z. Zhou  
Department of Orthopaedics  
Orthopaedic Research Institute  
West China Hospital  
Sichuan University  
Chengdu 610041, China  
E-mail: [luozzy@wchscu.edu.cn](mailto:luozzy@wchscu.edu.cn); [zhouzongke@scu.edu.cn](mailto:zhouzongke@scu.edu.cn)  
Z. Liang, L. Li  
West China School of Nursing  
Sichuan University  
Chengdu 610041, China

X. Rong  
Department of Medical Ultrasound  
West China Hospital  
Sichuan University  
Chengdu 610041, China  
G. Tang  
Guangzhou Municipal and Guangdong Provincial Key Laboratory of Molecular Target & Clinical Pharmacology  
the NMPA and State Key Laboratory of Respiratory Disease  
The Fifth Affiliated Hospital and School of Pharmaceutical Sciences  
Guangzhou Medical University  
Guangzhou 511436, China  
E-mail: [guoshengtang@gzhmu.edu.cn](mailto:guoshengtang@gzhmu.edu.cn)

 The ORCID identification number(s) for the author(s) of this article can be found under <https://doi.org/10.1002/sml.202403753>

DOI: 10.1002/sml.202403753

moisturization, and lubrication.<sup>[9]</sup> Although these barriers with different properties can be prepared in various forms (liquids, hydrogels, films, etc.), they exhibit a short residence time at the surgical site owing to their low tissue attachment capacity, which limits their in situ clinical efficacy.<sup>[10]</sup> To enhance attachment and retention on the target tissue, barriers with adhesive properties have attracted increased research interest. Catechol-based adhesive,<sup>[11,12]</sup> Schiff base reaction-based,<sup>[13]</sup> and non-covalent interaction-based strategies or combinations of these<sup>[14]</sup> have been applied to ensure firm adherence of barriers to the injured tissue. However, these barriers typically exhibit double-sided adhesive properties owing to a lack of structural heterogeneity, potentially resulting in undesired tissue attachment or additional adhesion formation with adjacent tissues, thereby compromising the barriers' anti-adhesion efficacy.<sup>[15,16]</sup>

Although Janus-structured barriers have attracted interest in terms of addressing the above contradiction between adhesion and anti-adhesion properties, their application, promotion, and translation in clinical surgery remain unsatisfactory. A few strategies have been proposed for fabricating hydrogels, electrospun films, and multi-layer composites with Janus structures using asymmetric coating,<sup>[17–20]</sup> unilateral ion sealing,<sup>[21,22]</sup> and solvent immersion methods.<sup>[23,24]</sup> However, the implantation of these complex Janus-structured barriers without injectability is difficult owing to the widespread adoption of minimally invasive surgery and the use of endoscopes. Additionally, these barriers often fail to perfectly cover irregularly shaped or folded tissues, which is common in surgeries involving soft tissues. Therefore, Janus-structured materials with injectability and asymmetric tissue adhesion capabilities are urgently needed to simultaneously ensure adhesion to the surgical site and isolation from the surrounding tissue.

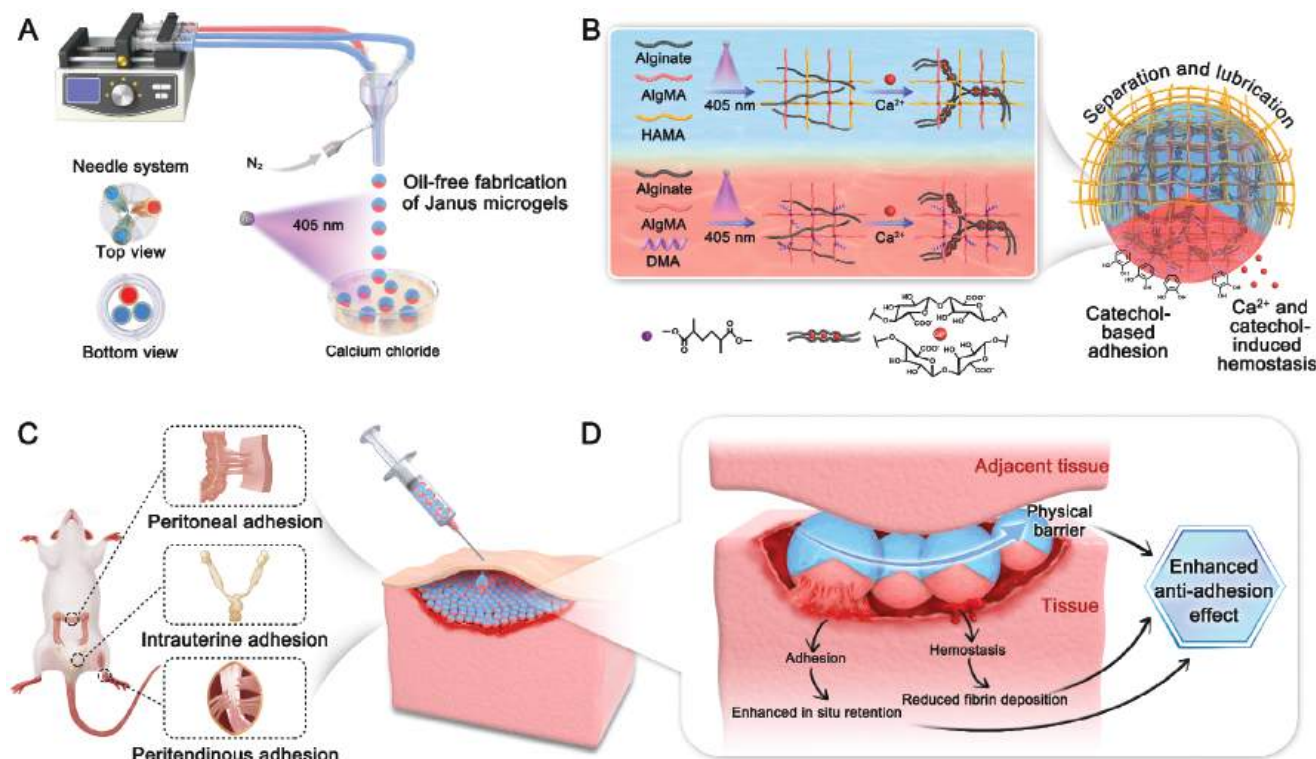
In our previous study, we established a novel oil-free gas-shearing microfluidic platform for producing bio-friendly multicompartimental alginate-based microgels.<sup>[25]</sup> To meet the clinical requirements of physical barriers for POA prevention, we further fabricated Janus-structured double-network microgels with asymmetric tissue adhesion capabilities using this platform. The anti-adhesive side of the Janus-MGs consisted of a double network comprising an ionic crosslinking network of  $\text{Ca}^{2+}$  and alginate and a photocrosslinking network of methacrylated alginate (AlgMA) and methacrylated hyaluronic acid (HAMA). Alginate, hyaluronic acid, and their derivatives can endow the Janus-MGs with effective anti-adhesion capability owing to their outstanding separation and lubrication properties.<sup>[26–29]</sup> The adhesive side of the Janus-MGs also consisted of a double network comprising an ionic crosslinking network of  $\text{Ca}^{2+}$  and alginate and a photocrosslinking network of AlgMA and dopamine methacrylamide (DMA). The catechol group in DMA provided the tissue attachment and retention capability for the Janus-MGs, thereby improving their in situ anti-adhesion capability.<sup>[30]</sup>  $\text{Ca}^{2+}$  and catechol-induced hemostasis can significantly accelerate local hemostasis, further enhancing the anti-adhesion capability of the Janus-MGs. Among the three most common POA models with distinct tissue structures and motion patterns, namely peritoneal adhesion, intrauterine adhesion, and peritendinous adhesion models, Janus-MGs exhibited excellent performance in preventing POA (Scheme 1). Therefore, the bio-friendly fabrication

strategy and the anti-adhesion effect enhanced by tissue adhesion and rapid hemostasis promote the use of Janus-MGs as a promising candidate for preventing POA following diverse surgical procedures.

## 2. Results and Discussion

### 2.1. Fabrication of Janus-MGs

In this study, the Janus-MGs were fabricated using a novel multi-channel gas-shearing microfluidic platform (Figures S1 and S2, Supporting Information). Under the driving force created by the nitrogen gas flow, the pre-gel solution formed small droplets with multiple compartments and then underwent polymerization in a collection petri dish (Scheme 1A). Platforms employing two, three, and four channels can fabricate microgels with two (Figure 1A-i), three (Figure 1B-i), and four compartments (Figure 1C-i), respectively. By encapsulating fluorescent dyes in the multi-compartment microgels, distinct boundaries at the interface between each compartment and the evenly distributed fluorescence in the microgels were observed under fluorescence microscopy and confocal laser scanning microscopy (CLSM) (Figures 1A-ii, B-ii, C-ii). After verifying the platform's ability to produce multi-compartment microgels, we further examined its effectiveness in preparing Janus-structured adhesive-anti-adhesive microgels. Two, three, and four-channel platforms were used to fabricate microgels with 1/2 adhesive side and 1/2 anti-adhesive side (Janus-MGs<sup>1/2</sup>), 1/3 adhesive side and 2/3 anti-adhesive side (Janus-MGs<sup>1/3</sup>), and 1/4 adhesive side and 3/4 anti-adhesive side (Janus-MGs<sup>1/4</sup>), respectively. Light microscopy images showed that all the Janus-MGs were well dispersed with intact morphological features and a distinct demarcation line between two sides (Figure 1A-iii, B-3iii, C-3iii). The particle sizes of Janus-MGs<sup>1/2</sup> (Figure 1A-iii), Janus-MGs<sup>1/3</sup> (Figure 1B-iii), and Janus-MGs<sup>1/4</sup> (Figure 1C-iii) were  $505.8 \pm 15.5 \mu\text{m}$ ,  $505.6 \pm 17.6 \mu\text{m}$ , and  $489.8 \pm 16.7 \mu\text{m}$ , respectively, and they were all distributed narrowly. The uniform and moderate sizes ensured the injectability of the microgels and, hence, enhanced their applicability.<sup>[31]</sup> Figure S3 (Supporting Information) shows the X-ray photoelectron spectroscopy (XPS) survey spectra in the presence of C, N, O, and Ca in the Janus-MGs. Given the consistent alginate content across different Janus-MGs, the Ca content remained consistent (ranging from 1.8% to 1.99% in different Janus-MGs) (Table S1, Supporting Information). The content of N was primarily influenced by the proportion of the adhesive side and the ratio of DMA used in the preparation of the different Janus-MGs (Table S1, Supporting Information). One-compartment microgels with anti-adhesive capability comprising alginate- $\text{Ca}^{2+}$ /AlgMA-HAMA were fabricated and named HAMA-MGs (Figure S4, Supporting Information), whereas those with adhesive capability comprising alginate- $\text{Ca}^{2+}$ /AlgMA-DMA were named DMA-MGs (Figure S5, Supporting Information). In addition, one-compartment microgels comprising alginate- $\text{Ca}^{2+}$  were fabricated as controls and named Alg-MGs, whereas Janus-MGs<sup>1/3</sup> was selected as the representative Janus-MGs for subsequent characterization.



**Scheme 1.** Janus-MGs for efficient prevention of POA. A) Equipment and fabrication of Janus-MGs. B) Double-crosslinking design of Janus-MGs and enhanced anti-adhesion efficacy of Janus-MGs. C,D) Janus-MGs efficiently prevent POA in rat peritoneal, intrauterine, and peritendinous adhesion models.

## 2.2. Characterization of Janus-MGs

Scanning electron microscopy (SEM) was performed to examine the surface morphology of the lyophilized microgels. HAMA-MGs and the anti-adhesive side of Janus-MGs<sup>1/3</sup> exhibited relatively smooth surfaces, whereas DMA-MGs and the adhesive side of Janus-MGs<sup>1/3</sup> had highly wrinkled and rough surfaces (Figure 2A). The different surface morphologies confirmed the successful fabrication of the Janus structure in Janus-MGs<sup>1/3</sup>, and these differences can be attributed to the different components and concentrations of the pre-gel solutions.<sup>[32]</sup> The lubrication performance of the microgels was tested using a tribometer (Figure 2B; Figure S6, Supporting Information). The 600 s friction test showed that Janus-MGs<sup>1/3</sup> had a significantly lower coefficient of friction (COF) (Figure 2C). The adhesion-enhanced lubrication of Janus-MGs<sup>1/3</sup> is advantageous for suppressing the activation of the mechanical stimulation–fibrous adhesion formation pathway induced by friction, thereby providing a better prevention effect against POA.<sup>[33–35]</sup> Janus-MGs<sup>1/3</sup> had the inherent injectable properties of hydrogel microspheres, allowing for ease of injection using a syringe without altering its morphology (Figure S7, Supporting Information), which ensured its delivery in minimally invasive surgery. In vitro degradation experiments showed that Janus-MGs<sup>1/3</sup> exhibited good degradability, with 80% weight loss within 7 days (Figure 2D). The in vivo degradation test also revealed that the volume of Janus-MGs<sup>1/3</sup> gradually decreased over time after subcutaneous implantation in rats, indicating gradual degradation of the micro-

gels. Remarkably, Janus-MGs<sup>1/3</sup> was nearly completely degraded after 7 days post-implantation (Figure S8, Supporting Information). The results of the degradation test are consistent with the optimal retention time to effectively prevent unwanted adhesion for 3–7 days, as reported in the literature.<sup>[26]</sup> As a physical barrier, good biocompatibility is an essential property requirement for microgels.<sup>[36,37]</sup> Therefore, Live/Dead staining and a cell counting kit-8 (CCK-8) assay were used to evaluate the effects of microgels on the viability and proliferation of MC3T3 cells in a Transwell co-culture system (Figure S9, Supporting Information). The results in Figure 2E,F and Figure S10 (Supporting Information) show that almost all the cells survived a three-day culture period without significant differences between the groups. The CCK-8 assay demonstrated that the number of cells in each group increased over time without significant differences, which is consistent with the Live/Dead staining results. In vivo, histological analysis of the surrounding skin tissue at the site of microgel implantation showed no significant tissue reaction and no significant difference compared with normal skin tissue after the degradation of microgels (Figure S11, Supporting Information). Furthermore, harvested organs (heart, liver, spleen, lung, and kidney) from the rats implanted with microgels showed no inflammatory cell infiltration or organic change, indicating satisfactory biocompatibility (Figure S12, Supporting Information). These results show that Janus-MGs<sup>1/3</sup> exhibited favorable biocompatibility and can serve as a physical barrier that provides a prevention effect at the surgical site in the body. For microgels with complex structures, the fabrication

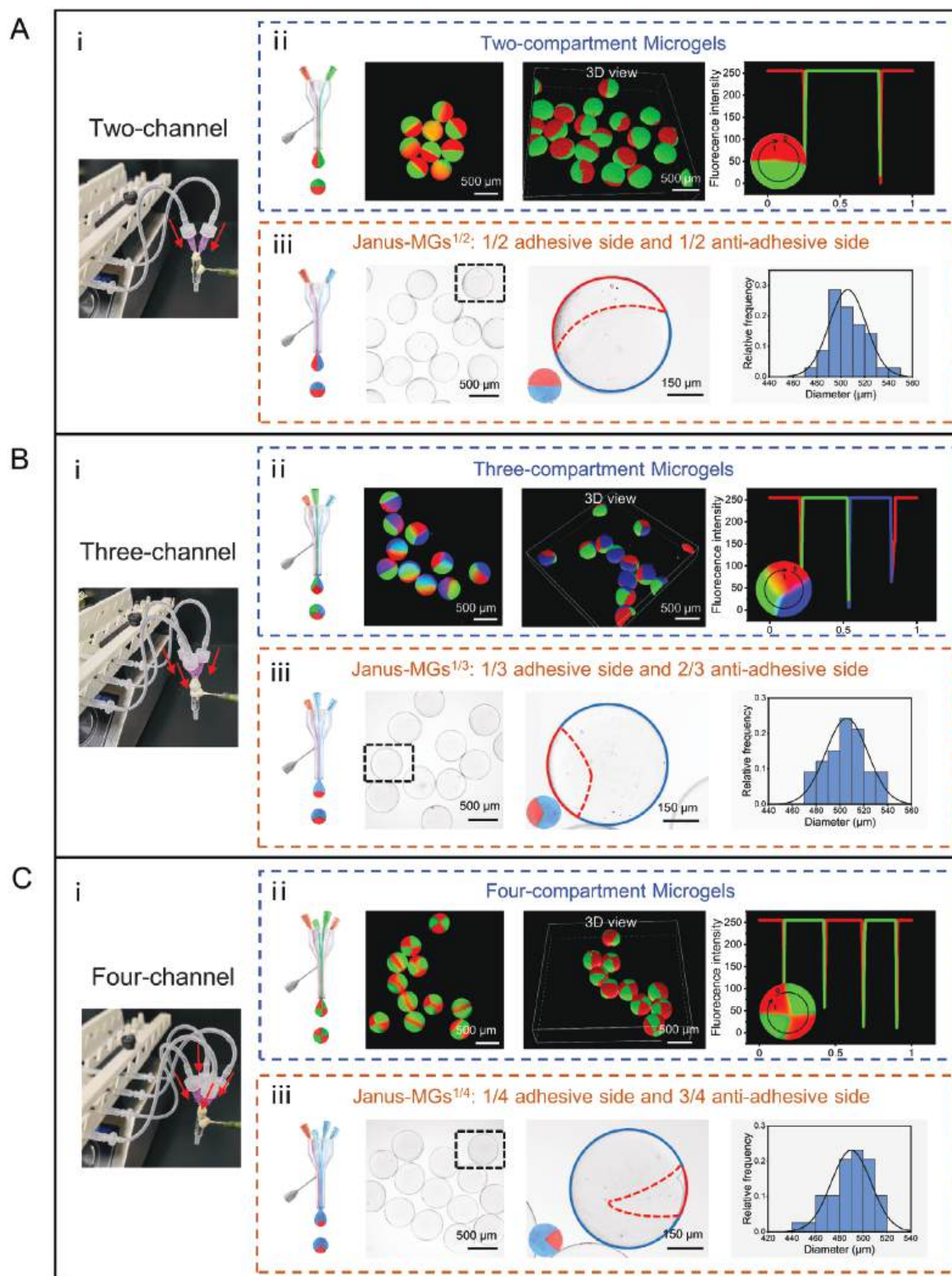


**Figure 1.** Fabrication of Janus-MGs. A-i) The equipment of two-channel microfluidic platform. Red arrows show the flow direction of pre-gel solution. A-ii) Fabrication scheme, fluorescence microscopy observation, CLSM observation, and fluorescence distribution of two-compartment microgels. For the line in the fluorescence distribution plot, the starting point is 0 and the end point is 1, as indicated in the circle shown in the representative fluorescent microgel. A-iii) Fabrication scheme, light microscopy observation, enlarged image of light microscopy observation, and size distribution of Janus-MGs<sup>1/2</sup>. B-i) Three-channel platform, B-ii) three-compartment microgels, and B-iii) Janus-MGs<sup>1/3</sup>. C-i) Four-channel platform, C-ii) four-compartment microgels, and C-iii) Janus-MGs<sup>1/4</sup>.

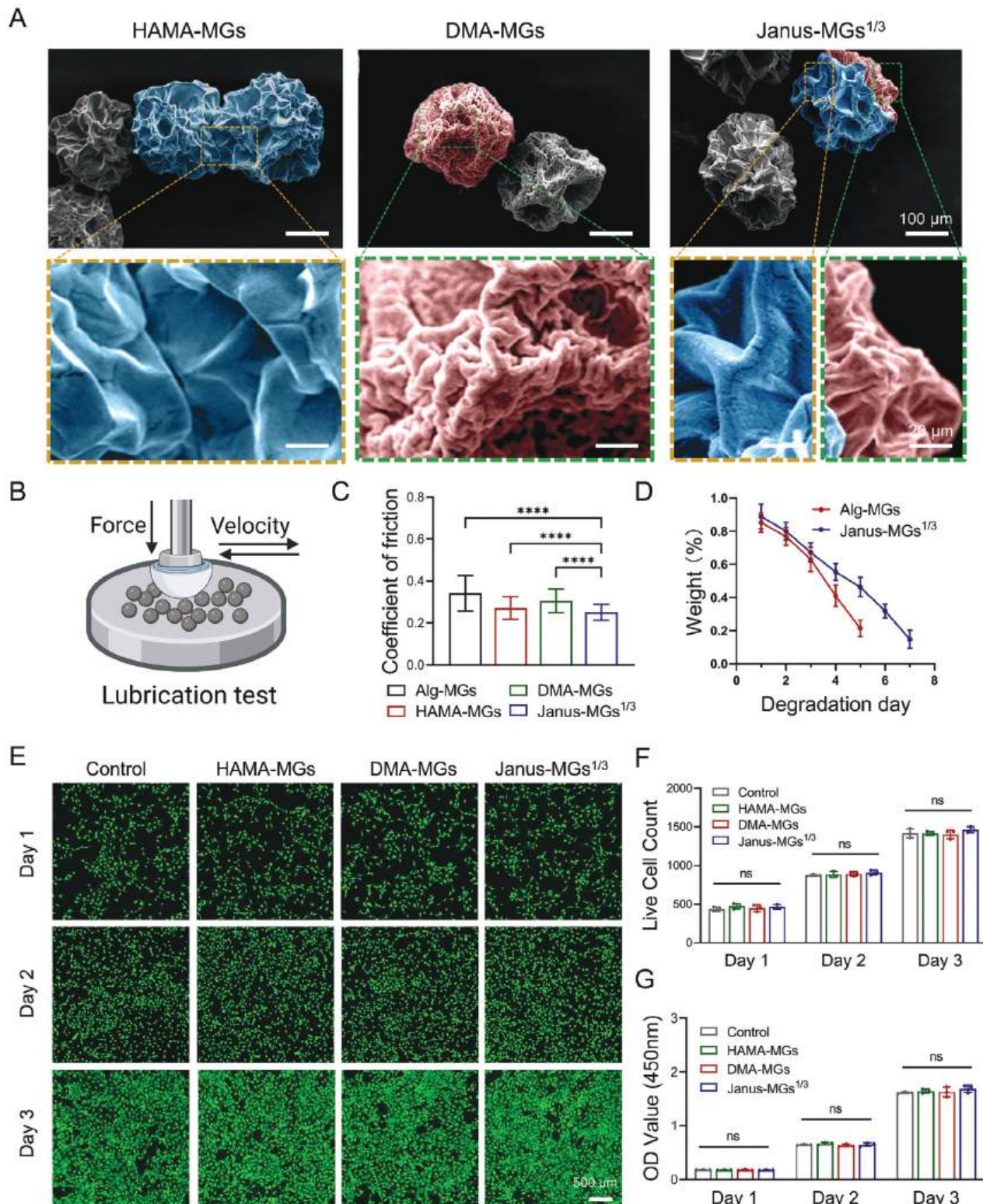


**Figure 2.** Characterization of Janus-MGs. A) SEM images and corresponding enlarged views. In Janus-MGs<sup>1/3</sup> observation, the yellow square refers to the anti-adhesive side and the green square refers to the adhesive side. B) Schematic illustration of lubrication test for measuring the COF of microgels using a tribometer. C) COF histograms for Alg-MGs, HAMA-MGs, DMA-MGs, and Janus-MGs<sup>1/3</sup> in the lubrication test. \*\*\*\* means  $p < 0.0001$ . D) The degradation curves of microgels.  $n = 3$  per group. E) Live (green)/Dead (red) staining for MC3T3 cells cocultured with microgels for 1, 2, and 3 days. F) Quantitative analysis of the live cell counts in Live/Dead staining. ns means no significant difference.  $n = 3$  per group. G) CCK-8 assay of MC3T3 cells cocultured with microgels for 1, 2, and 3 days. ns means no significant difference.  $n = 3$  per group.

technique, hydrogel prepolymer selection, and crosslinking mechanism often negatively affect their biocompatibility, thereby limiting their application in the biomedical field.<sup>[38]</sup> The fabrication strategy of these integrally formed Janus-MGs offers biocompatibility and feasibility in clinical translation owing to their oil-free fabrication method and the use of biocompatible polysaccharides.

### 2.3. Adhesion Capacity Test

An *in vivo* adhesion capacity test was designed to evaluate the adhesion capacity of the microgels on the abdominal wall, cecum, and tendon of rats. After anesthetizing the rats, a wound was created on the surface of the tissues to mimic damage to the surgical area (Figures S13 and S14, Supporting Information). The microgels were then applied, and the surrounding tissue of the wound was rubbed back and forth to simulate mutual movement between tissues in the body (Figure 3A). In the rat's abdominal wall injury model, the average adhesion rates of DMA-MGs, Janus-MGs<sup>1/2</sup>, and Janus-MGs<sup>1/3</sup> were 68.7%, 60.6%, and 53.0%, respectively, which are comparable among the groups and significantly higher than those of the Janus-MGs<sup>1/4</sup> and HAMA-MGs (28.0% and 10.2%, respectively) (Figure 3B). In the cecum injury model, the average adhesion rates of DMA-MGs, Janus-MGs<sup>1/2</sup>, and Janus-MGs<sup>1/3</sup> were 84.6%, 82.5%, and 75.7%, respectively, which are comparable among the groups and significantly higher than those of the Janus-MGs<sup>1/4</sup> and HAMA-MGs groups (55.9% and 23.0%, respectively) (Figure 3C). In the rat's tendon, the average adhesion rates of DMA-MGs, Janus-MGs<sup>1/2</sup>, and Janus-MGs<sup>1/3</sup> were 87.1%, 79.3%, and 72.8%, respectively, which are comparable among the groups and significantly higher than those of the Janus-MGs<sup>1/4</sup> and HAMA-MGs groups (52.7% and 24.1%, respectively) (Figure 3D). Therefore, DMA-MGs, Janus-MGs<sup>1/2</sup>, and Janus-MGs<sup>1/3</sup> exhibited similar high adhesion capabilities in rat tissues and were significantly superior to those of Janus-MGs<sup>1/4</sup> and HAMA-MGs, both of which had low adhesion capabilities (Figure 3E). We finally selected Janus-MGs<sup>1/3</sup> as the representative Janus-MGs for subsequent *in vivo* studies as it achieved a higher adhesion capacity with a small adhesive side proportion, demonstrating a higher adhesion efficiency and balance between adhesion capacity and anti-adhesion capacity (Figure 3F). The possible adhesion behavior of Janus-MGs<sup>1/3</sup> on the tissue involves rolling of Janus-MGs<sup>1/3</sup>. Initially, the orientation of the Janus-MGs<sup>1/3</sup> on the tissue surface is random after application. When subjected to external forces on the tissue surface, the adhesive side of Janus-MGs<sup>1/3</sup> is more prone to interact with the wound, thereby achieving catechol-based adhesion (Figure 3G).

### 2.4. In Vivo Hemostatic Performance

Given that the formation of blood clots and insoluble fibrin deposition following coagulation are fundamental to fibrous adhesion formation, excellent hemostatic performance can significantly enhance the POA prevention effect of anti-adhesion materials.<sup>[6,7]</sup> In this study, the *in vivo* hemostatic performance of microgels was investigated in a rat liver hemorrhage and

hemostasis model (Figure 4A) and a rat tail amputation hemorrhage and hemostasis model (Figure 4B). As a visceral organ with an abundant blood supply, the liver is prone to profuse bleeding and difficult hemostasis during abdominal surgeries.<sup>[39]</sup> Immediately after making an incision on the liver, Janus-MGs<sup>1/3</sup> were applied to the wound surface and firmly adhered to the bleeding site (Figure S15, Supporting Information). Only 173.3 ± 45.1 mg of blood was lost, and hemostasis occurred within 34.7 ± 15.3 s (Figure 4C–E and Movie S1, Supporting Information). In contrast, the control group without any hemostatic treatment achieved hemostasis only after a blood loss of 736.7 ± 140.1 mg and a bleeding time of 286.0 ± 48.1 s (Figure 4C–E and Movie S2, Supporting Information). HAMA-MGs took 128.0 ± 33.1 s to achieve hemostasis with a blood loss of 443.3 ± 70.2 mg, which is significantly higher than that of Janus-MGs<sup>1/3</sup> but lower than that of the control group (Figure 4C–E). When DMA-MGs were applied, the microgels also adhered to the bleeding site (Figure S15, Supporting Information) and exhibited a comparable hemostatic effect to that of Janus-MGs<sup>1/3</sup>, with a blood loss of 183.3 ± 49.3 mg and a bleeding time of 20.7 ± 6.1 s (Figure 4C–E).

The tail amputation hemorrhage and hemostasis model is a commonly used hemostasis model and involves damage to various tissues, including skin, bone, connective tissue, and large blood vessels, posing significant challenges to the effective hemostatic performance of materials.<sup>[40]</sup> In the tail amputation model, the control group still exhibited the highest blood loss (953.3 ± 140.5 mg) and the longest time to achieve hemostasis (316.0 ± 42.6 s) (Figure 4F–H and Movie S3, Supporting Information). HAMA-MGs exhibited a blood loss of 566.7 ± 85.1 mg and a bleeding time of 191.3 ± 35.9 s, which are significantly lower than those of the control group but higher than those of the Janus-MGs<sup>1/3</sup> group (Figure 4F–H). This moderate hemostatic effect of HAMA-MGs can be attributed to the Ca<sup>2+</sup> in alginate-Ca<sup>2+</sup> activating the endogenous coagulation pathway.<sup>[41,42]</sup> The DMA-MGs and Janus-MGs<sup>1/3</sup> groups exhibited significantly reduced blood loss (140.0 ± 81.9 and 193.3 ± 116.8 mg, respectively) and bleeding time (43.7 ± 25.4 and 55.3 ± 27.6 s, respectively), with no statistical difference between the groups (Figure 4F–H and Movie S4, Supporting Information). DMA-MGs and Janus-MGs<sup>1/3</sup> groups also exhibited similar adhesion behavior and sealing effects on the incision, unlike HAMA-MGs that were easily dispersed by blood flow (Figure S16, Supporting Information). The excellent hemostatic properties of DMA-MGs and Janus-MGs<sup>1/3</sup> can be attributed to the synergistic effects of adhesion-based wound closure, hydrogen bonding, hydrophobic interactions between the catechol group and serum proteins,<sup>[43,44]</sup> and Ca<sup>2+</sup>-activated coagulation<sup>[41,42]</sup> (Figure 4I).

### 2.5. In Vivo Prevention of Peritoneal Adhesion

To comprehensively evaluate the efficacy of Janus-MGs<sup>1/3</sup> for preventing POA following diverse surgical procedures, this study selected three tissues and models that are most prone to POA in clinical practice, each with different motion patterns and tissue structures. These included a peritoneal adhesion model involving the intestine and abdominal wall, which are two distinct

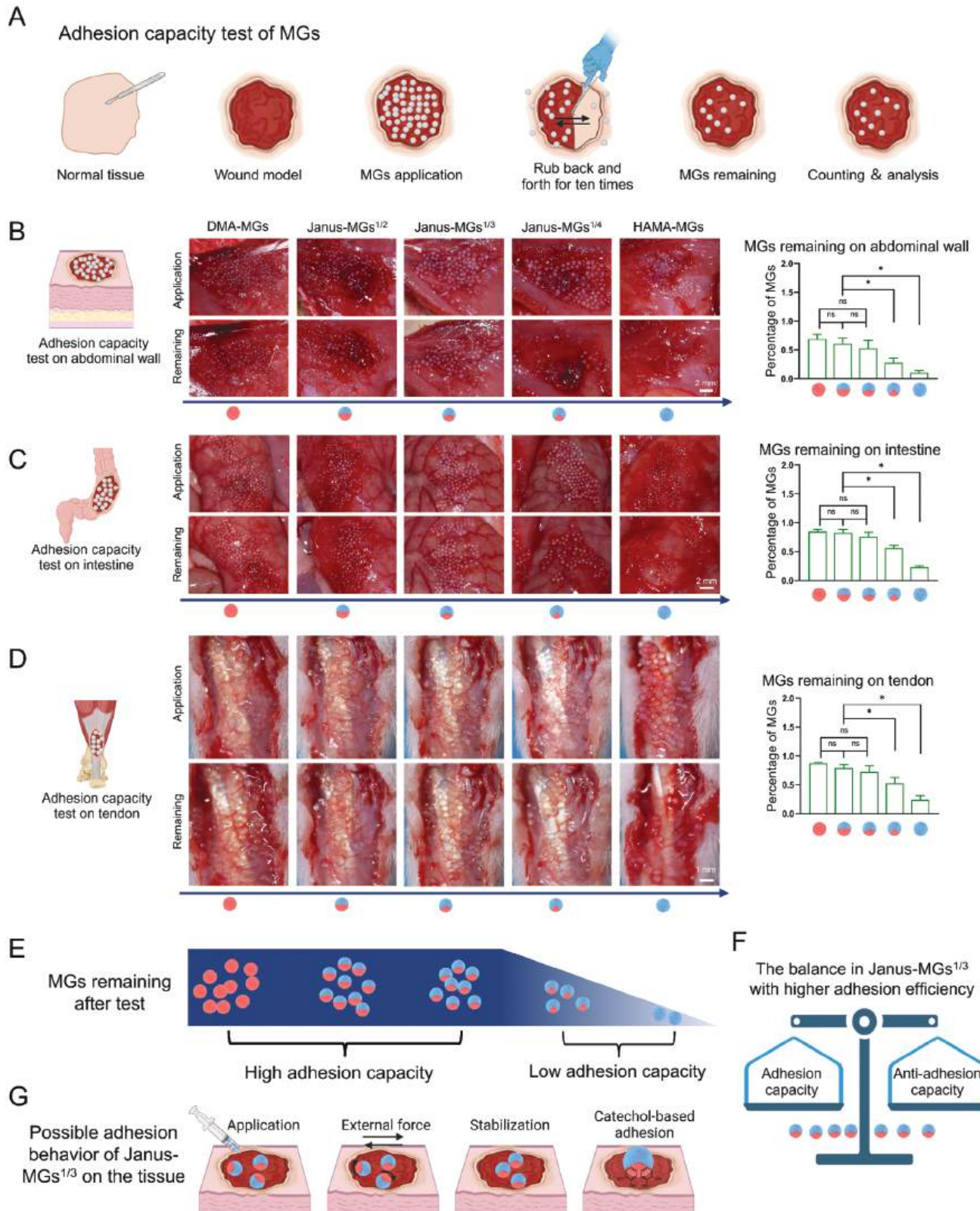


**Figure 3.** Adhesion capacity test of Janus-MGs. A) Schematic illustration of in vivo adhesion capacity test of microgels. B–D) Adhesion capacity tests of microgels in the rat's abdominal wall injury model, intestine injury model, and tendon model, respectively. \* means  $p < 0.05$  and ns means no significant difference.  $n = 3$  per group. E) Microgels remaining after the test and adhesion capacity according to the adhesion capacity test. F) Janus-MGs<sup>1/3</sup> demonstrate higher adhesion efficiency and a balance between adhesion capacity and anti-adhesion capacity. G) Schematic illustration of the possible adhesion behavior of Janus-MGs<sup>1/3</sup>. MG: microgels.

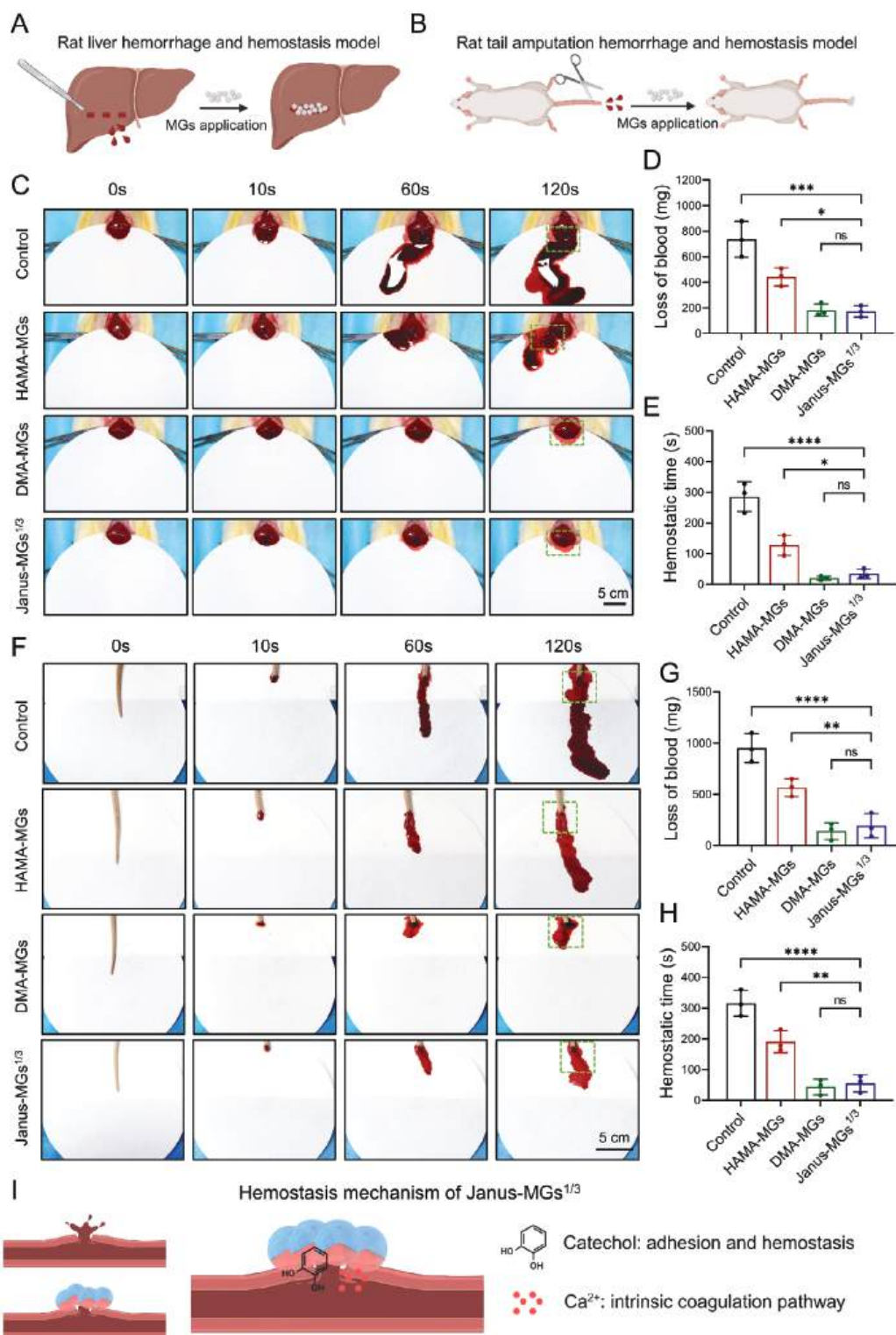


**Figure 4.** In vivo hemostatic performance of Janus-MGs. A) Schematic illustration of hemostatic capacity test of microgels in rat liver hemorrhage and hemostasis model. B) Schematic illustration of hemostatic capacity test of microgels in rat tail amputation hemorrhage and hemostasis model. C) Photographs of hemostatic test in the rat liver hemorrhage and hemostasis model. D,E) Blood loss and hemostatic time for different treatments in the rat liver hemostasis model. \* means  $p < 0.05$ . \*\*\* means  $p < 0.001$ . \*\*\*\* means  $p < 0.0001$ . ns means no significant difference. n = 3 per group. F) Photographs of hemostatic test in the rat tail hemorrhage and hemostasis model. G,H) Blood loss and hemostatic time for different treatments in the rat tail hemostasis model. \*\* means  $p < 0.01$ . \*\*\*\* means  $p < 0.0001$ . ns means no significant difference. n = 3 per group. I) The potential hemostatic mechanism of Janus-MGs<sup>1/3</sup>. MG: microgels.

tissues characterized by peristaltic motion; an intrauterine adhesion model involving the uterus, a hollow organ characterized by a static state motion pattern; and a peritendinous adhesion model involving the tendon and the surrounding tissue, which are adjacent organs characterized by repetitive friction.

Peritoneal adhesion, which affects up to 90% of patients who undergo abdominal surgery, can lead to significant abdominal pain, intestinal obstruction, organ dysfunction, and other serious adverse outcomes.<sup>[45,46]</sup> In this study, a rat peritoneal adhesion model was established by abrasion and excising defects on the cecum and the adjacent abdominal wall (Figures S13 and S14, Supporting Information). Janus-MGs<sup>1/3</sup> were applied to both traumatized surfaces during surgery. The control group without any anti-adhesion treatment exhibited severe peritoneal adhesion on gross observation and the highest adhesion score on days 7 and 14 after surgery, confirming the successful establishment of the model (Figure 5A–D).<sup>[47]</sup> Attenuated adhesion between the abdominal wall and cecum and a lower adhesion score were observed in the HAMA-MGs group (Figure 5A–D), which can be attributed to the physical barrier effect of HAMA, alginate, and AlgMA in HAMA-MGs.<sup>[48]</sup> However, the low tissue adhesion ability and short residence time of HAMA-MGs limits their adhesion prevention efficacy, particularly within the abdominal cavity, which has ample space and is where organs are in a state of constant mutual movement.<sup>[12]</sup> For the DMA-MGs group, the double-sided adhesive property compromised the anti-adhesion efficacy, resulting in a slightly lower score compared with that of the control group (Figure 5A–D). In contrast, the Janus-MGs<sup>1/3</sup> group demonstrated complete prevention for POA and the lowest mean adhesion score close to zero on days 7 and 14 after surgery (Figure 5A–D), which demonstrates the effectiveness of our strategy for enhancing the anti-adhesion efficacy of the physical barrier by imparting asymmetric tissue adhesion capability to Janus-structured materials. The findings from histological staining supported the gross observation and scores (Figure 5A–D). Hematoxylin eosin (HE) and Masson staining showed that the control group had an obvious adhesion area with extensive collagen deposition between the injured abdominal wall and cecum. The occurrence of adhesion in the HAMA-MGs and DMA-MGs groups can also be observed; however, the density of collagen in the adhesion area was lower compared with that of the control group. Significant inflammatory cell infiltration can be observed in the three aforementioned groups. For the Janus-MGs<sup>1/3</sup> group, the histology for the injured abdominal wall and cecum can only be performed separately and combined in one image because no adhesion developed between the abdominal wall and cecum (Figure 5A,B).<sup>[49]</sup> The findings for the Janus-MGs<sup>1/3</sup> group were highly similar to those of the normal tissue (Figure S17A–C, Supporting Information) without adhesion or connective tissues, collagen deposition, or inflammatory cell infiltration. Compared with other forms of physical barriers such as commercialized films (Seprafilm, Sanofi, Paris, France),<sup>[50]</sup> liquids (Adept, Baxter, Unterschleissheim, Germany),<sup>[51]</sup> and hydrogels (Hyalobarrier, Anika Therapeutics, S.r.l., Abano Terme, Italy),<sup>[52]</sup> Janus-MGs<sup>1/3</sup> were more easily delivered, had a longer retention time in situ, possessed a Janus structure, and, hence, exhibited superior anti-adhesion effect.

## 2.6. In Vivo Prevention of Intrauterine Adhesion

Intrauterine adhesion caused by endometrial damage, resulting in adhesion or even obliteration of the uterine cavity, will severely affect women's reproductive capacity and impose a significant psychological burden on the patient.<sup>[53,54]</sup> In this study, a rat intrauterine adhesion model established by mechanical endometrial injury was used to determine the efficacy of Janus-MGs<sup>1/3</sup> for preventing adhesion following intrauterine surgery. After modeling bilateral uterine cavities, microgels were applied to the right side of the uterus, whereas the left side received no anti-adhesion treatment, allowing for a better comparison of efficacy through self-control.<sup>[55]</sup> On day 7 after surgery, severe contraction and hydrometra of the uterus were observed in the control, HAMA-MGs, and DMA-MGs groups, suggesting intrauterine adhesion formation and HAMA-MGs and DMA-MGs were ineffective for adhesion prevention (Figure 6A). Notably, structural deformation of the uterus was mild in the Janus-MGs<sup>1/3</sup> group, which is highly similar to that of the sham group. The severity of intrauterine adhesion on gross observation appeared to have decreased on day 14 after surgery (Figure 6A). Furthermore, we examined the intrauterine adhesion formation by histological staining. Partial obliteration of the uterine cavity, loss of endometrial epithelium, and collagen fiber replacement in the endometrium were observed in the control group (Figure 6B,C). The HAMA-MGs and DMA-MGs groups exhibited a partial reduction in the formation of adhesion. The Janus-MGs<sup>1/3</sup> group showed unreduced uterine cavity with endometrial regeneration close to that of the sham group (Figure 6B,C; Figure S18, Supporting Information). Quantitative analysis of the number of glands and endometrial thickness in HE and Masson staining further supported these findings. The Janus-MGs<sup>1/3</sup> group had the highest number of glands and endometrial thickness compared with those of the other groups, highlighting the improved endometrial repair and uterine function obtained by applying Janus-MGs<sup>1/3</sup> (Figure 6D,E).<sup>[56]</sup> Ensuring the long-term retention and effectiveness of anti-adhesion materials after implantation in the uterine cavity, a hollow organ is a well-known problem.<sup>[54,57]</sup> Additionally, the intrauterine adhesion prevention materials should facilitate convenient delivery to the uterine cavity and avoid causing pain when passing through the narrow cervical orifice.<sup>[58]</sup> The injectable Janus-MGs with asymmetric tissue adhesion capabilities proposed in this study address these issues: Janus-MGs<sup>1/3</sup> can adhere to the side of uterine wall and can achieve separation and lubrication in the uterine cavity. Janus-MGs<sup>1/3</sup> simultaneously ensured ease of detachment of materials and addressed the issue of undesired adhesion formation in double-sided adhesive materials (Figure 6F).

## 2.7. In Vivo Prevention of Peritendinous Adhesion

Surgical repair of tendon injuries often leads to bleeding, inflammation, and fibrinolysis, ultimately resulting in peritendinous adhesion formation and limb motor dysfunction.<sup>[59]</sup> In this study, a rat peritendinous adhesion model was established to evaluate the adhesion prevention efficacy of Janus-MGs<sup>1/3</sup> in a musculoskeletal system with high activity levels.<sup>[60]</sup> In the control group, the repaired site of the tendon formed extensive dense

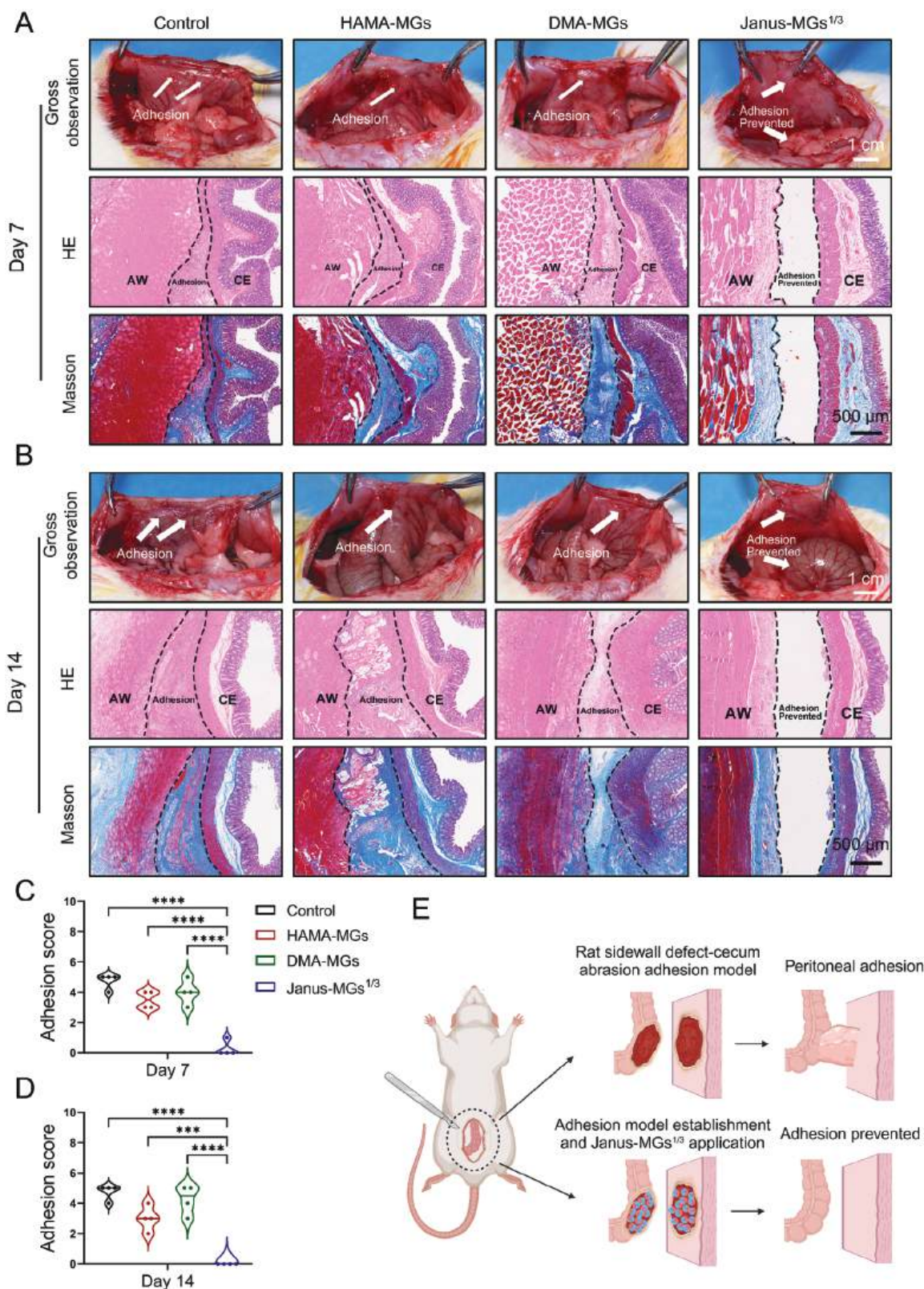


**Figure 5.** Janus-MGs for the prevention of POA in a rat peritoneal adhesion model. A,B) Gross observation, HE staining and Masson staining for the evaluation of peritoneal adhesion on postoperative days 7 and 14. White arrows show the adhesion between the abdominal wall and the cecum in gross observation. AW: abdominal wall. CE: cecum. C,D) Adhesion scores in gross observation on days 7 and 14. \*\*\* means  $p < 0.001$ . \*\*\*\* means  $p < 0.0001$ .  $n = 4$  per group. E) Schematic illustration of peritoneal adhesion prevention effect of Janus-MGs<sup>1/3</sup>.

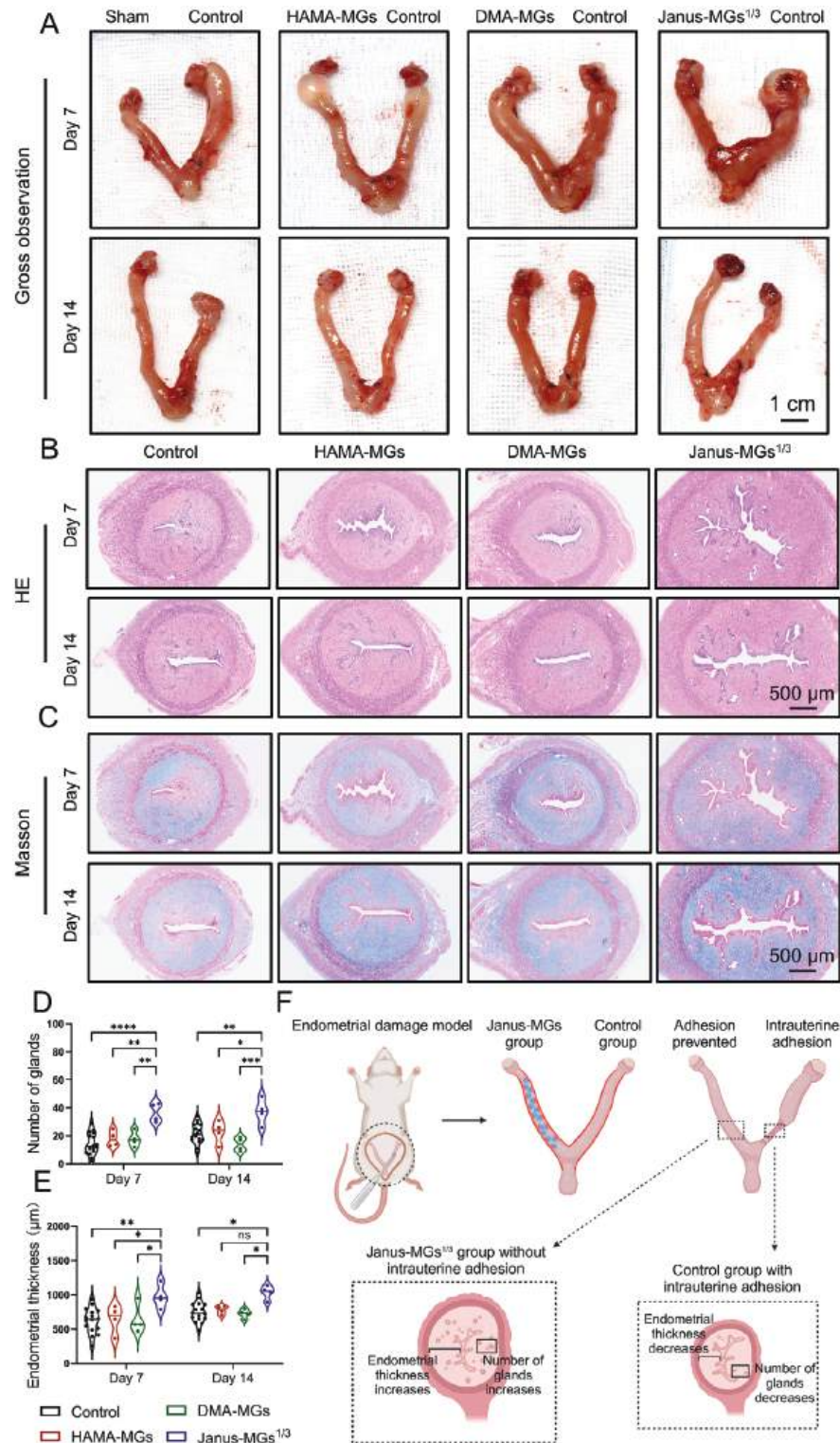


**Figure 6.** Janus-MGs for the prevention of POA in a rat intrauterine adhesion model. A) Gross observation of intrauterine adhesion on postoperative days 7 and 14. B) HE staining for the evaluation of intrauterine adhesion on postoperative days 7 and 14. C) Masson staining for the evaluation of intrauterine adhesion on postoperative days 7 and 14. D) Number of glands in histological evaluation on days 7 and 14. \* means  $p < 0.05$ . \*\* means  $p < 0.01$ . \*\*\* means  $p < 0.001$ . \*\*\*\* means  $p < 0.0001$ .  $n = 16$  for control group and  $n = 4$  for other groups. E) Endometrial thickness in histological evaluation on days 7 and 14. \* means  $p < 0.05$ . \*\* means  $p < 0.01$ . ns means no significant difference.  $n = 16$  for control group and  $n = 4$  for other groups. F) Schematic illustration of intrauterine adhesion prevention effect of Janus-MGs<sup>1/3</sup>.

adhesion with the surrounding tissues on days 14 and 21 after the surgery, which was difficult to dissect (Figure 7A–B). In contrast, the repaired tendon exhibited a relatively smooth and glossy morphology in the Janus-MGs<sup>1/3</sup> group, with far less fibrous adhesion formation, similar to the normal tendon tissue (Figure 7A,B; Figure S19, Supporting Information). The macroscopic adhesion score showed that the Janus-MGs<sup>1/3</sup> group had the lowest adhesion score, whereas the HAMA-MGs group had a partially decreased score compared with that of the control group (Figure 7C). This indicates that the barrier effect of HAMA-MGs can provide a certain anti-adhesion effect on the injured tendon; however, the repeated mutual movement between the tendon and the surrounding tissues significantly weakens this benefit. Because of the potential for unexpected and undesirable adhesion formation, the DMA-MGs group had a high macroscopic adhesion score (Figure 7C). The representative histological results of peritendinous adhesion around the repaired tendon on days 14 and 21 after surgery are shown in Figure 7A,B. The Janus-MGs<sup>1/3</sup> group demonstrated a physiological space between the tendon and the surrounding tissues, indicating the mildest adhesive condition. Large areas of adhesion were observed around the repaired tendon, with fibrous tissue invading the repaired tendons in the control, HAMA-MGs, and DMA-MGs groups. The histological adhesion-graded evaluation showed that the Janus-MGs<sup>1/3</sup> group had the lowest degree of adhesion compared with those of other groups (Figure 7D). As one of the body's primary motor organs, tendons often experience displacement of implanted hydrogels owing to long-term repetitive friction against surrounding tissues.<sup>[61]</sup> The asymmetrical adhesiveness of Janus-MGs<sup>1/3</sup> ensures their adhesion to injured tendons or surrounding tissues while providing separation and lubrication on the other side (Figure 7E). The presence of a lubricating protective layer around the tendon can also reduce friction during tendon movement and promote rapid repair of injured tendons.<sup>[33,62]</sup> Compared with other forms of physical barriers, such as membrane,<sup>[63]</sup> liquid,<sup>[64]</sup> and hydrogel,<sup>[60]</sup> the Janus-MGs<sup>1/3</sup> proposed in this study exhibited improved deliverability, prolonged retention time, superior Janus structure, and an enhanced anti-adhesion effect.

Overall, Janus-MGs with asymmetric tissue adhesion capabilities were fabricated using a novel gas-shearing microfluidic platform in this study. The bio-friendly microgel fabrication strategy, including the oil-free gas-shearing method and choice of natural hydrogel prepolymers, ensured their biocompatibility and application in the biomedical field. For the in vivo models, Janus-MGs exhibited remarkable performances in terms of tissue adhesion and hemostasis. Three POA models that are prevalent in clinical practice were established to evaluate the efficacy of Janus-MGs for preventing POA, including peritoneal, intrauterine, and peritendinous adhesion, with each characterized by distinct tissue motion patterns and structural properties. Our findings show that Janus-MGs with enhanced anti-adhesion effects from tissue adhesion and rapid hemostasis effectively prevented adhesion formation in all the models. These results demonstrated the potential of Janus-MGs as a reliable and promising candidate for preventing POA following diverse surgical procedures. This study offers an alternative strategy for fabricating Janus-structured materials for POA prevention.

### 3. Experimental Section

**Multi-Channel Gas-Shearing Microfluidic Platform:** The gas-shearing microfluidic platform mainly consists of five parts: an electronic syringe pump for providing pre-gel solutions; a nitrogen cylinder supplying nitrogen gas, regulated using a flowmeter to control the gas flow rate; a custom-made multi-channel coaxial needle system with 30G inner needles inserted into an outer needle for transporting liquids and a 14G needle for transporting nitrogen gas; a collection bath containing a CaCl<sub>2</sub> solution (C299717, Aladdin); and an ultraviolet light source irradiating the microgels in the bath. The equipment for Janus-MGs fabrication is shown in Figures S1 and S2 (Supporting Information).

**Fabrication of Janus-MGs:** The pre-gel solution for the fabrication of the anti-adhesive side of Janus-MGs consisted of 1.5% (w/v) alginate (A2033, Sigma-Aldrich), 1% (w/v) AlgMA, 2% (w/v) HAMA, and 0.3% (w/v) lithium phenyl(2,4,6-trimethylbenzoyl) phosphinate (LAP; Engineering for Life). The pre-gel solution for the fabrication of the adhesive side of Janus-MGs consisted of 1.5% (w/v) alginate, 2% (w/v) AlgMA, 3% (w/v) DMA (N303773, Aladdin), and 0.3% (w/v) LAP. The synthesis of AlgMA followed the procedures as previously described.<sup>[65]</sup> In Brief, 1 g alginate was dissolved fully in 100 mL of DI water at 4 °C. A total of 30 mL methacrylic anhydride (276685, Sigma-Aldrich) was added dropwise to the solution under vigorous stirring. The pH of the solution was regulated to ≈ 8 with 0.5 M sodium hydroxide solution periodically. The reaction was kept at 4 °C under vigorous stirring for 48 h. Then the solution was dialyzed against DI water using dialysis membrane (Mw cut off: 12–14 kDa) for 7 days to remove excess methacrylic anhydride. The purified AlgMA was obtained by lyophilization. HAMA was synthesized according to previously reported protocols with modifications.<sup>[66]</sup> Briefly, 1 g hyaluronic acid (Macklin, H909937) was dissolved fully in 100 mL of DI water at 4 °C. A total of 10 mL methacrylic anhydride was added to the solution slowly under vigorous stirring and the solution was regulated to pH 8 with sodium hydroxide solution periodically. The reaction was kept at 4 °C under vigorous stirring for 48 h. Then the solution was dialyzed against DI water for 7 days and the purified HAMA was obtained by lyophilization.

Two types of pre-gel solutions were pumped into different channels, and the number of channels transporting the two solutions determined the volume ratio of the adhesive and anti-adhesive sides of Janus-MGs. The number ratios of channels transporting adhesive pre-gel solution and anti-adhesive pre-gel solution were 1:0, 1:1, 1:2, 1:3, and 0:1 for the fabrication of DMA-MGs, Janus-MGs<sup>1/2</sup>, Janus-MGs<sup>1/3</sup>, Janus-MGs<sup>1/4</sup>, and HAMA-MGs, respectively. To visualize the Janus structure in the microgels, 0.2% (w/v) fluorescent polystyrene nanoparticles (red, green, and blue; 200 nm, Xi'an Ruixi) were added to the pre-gel solution. The flow rate of the pre-gel solution was set at 1 mL h<sup>-1</sup>. The flow rate of nitrogen gas was set at 5 L min<sup>-1</sup> to provide the shear force for forming the microdroplets. In the collection bath, 2% (w/v) CaCl<sub>2</sub> was used for ionic crosslinking of microgels, and UV light (405 nm) was used for photocrosslinking for 5 min. The microgels were then collected and washed three times with 1X phosphate-buffered saline (HyClone). Before applying the microgels, the excess water in the interstitial spaces between the microgels was removed.

**Characterization of Janus-MGs:** The fluorescence-labeled microgels were observed under inverted fluorescence microscopy and CLSM (N-SIM S Nikon) to show the multiple compartments. The morphology of the Janus-MGs was observed under inverted light microscopy, and the sizes of the microgels were measured using ImageJ software. XPS was used to investigate the composition of microgels. SEM was used to observe the morphology of the lyophilized microgels.

**Tribological Test:** A tribological test was conducted using a multifunction tribometer (MFT-5000, Rtec instruments) based on a previously reported protocol.<sup>[67]</sup> During reciprocating sliding, a zirconium oxide sphere and a zirconium oxide disk were used as the top and bottom surfaces, respectively. Next, 10 mg of microgels in PBS was dropped on the disk, and the test was carried out for 600 s. The oscillation amplitude, frequency, and load were set as 4 mm, 1 Hz, and 1N, respectively.

**In Vitro Degradation and Biocompatibility:** For in vitro degradation test, 100 mg of microgels were incubated in a 2 mL sterile PBS solution containing 5 mg mL<sup>-1</sup> hyaluronidase (Engineering for Life). The solution was

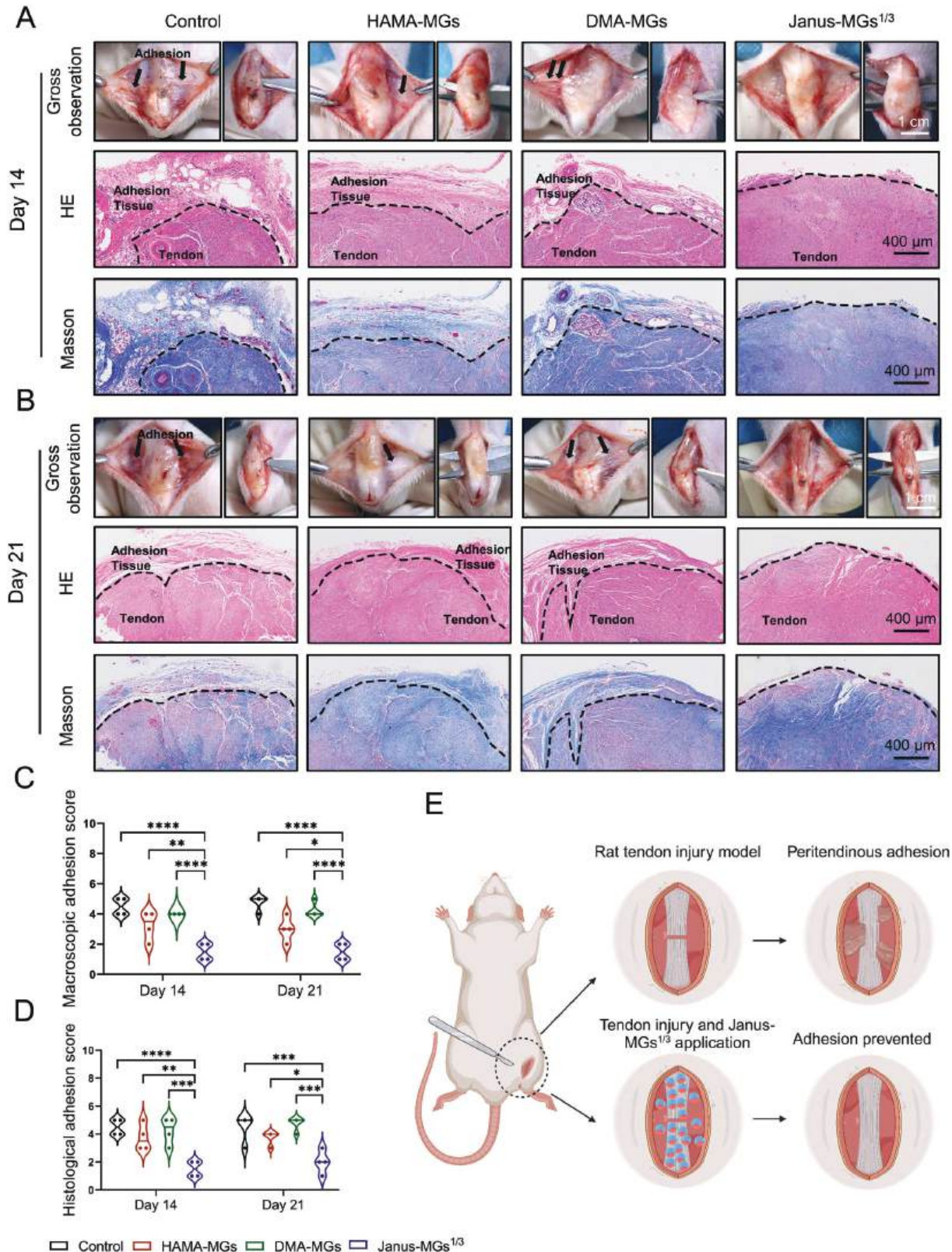


**Figure 7.** Janus-MGs for the prevention of POA in a rat peritendinous adhesion model. A,B) Gross observation, HE staining and Masson staining for the evaluation of peritendinous adhesion on postoperative days 14 and 21. Black arrows show the adhesion between the tendon and surrounding tissue on gross observation. C) Macrosopic adhesion scores on postoperative days 14 and 21. \* means  $p < 0.05$ . \*\* means  $p < 0.01$ . \*\*\*\* means  $p < 0.0001$ .  $n = 4$  per group. D) Histological adhesion scores on postoperative days 14 and 21. \* means  $p < 0.05$ . \*\* means  $p < 0.01$ . \*\*\* means  $p < 0.001$ . \*\*\*\* means  $p < 0.0001$ .  $n = 4$  per group. E) Schematic illustration of peritendinous adhesion prevention effect of Janus-MGs<sup>1/3</sup>.

agitated in a shaker at a temperature of 37 °C and refreshed every day. The microgels were weighed every day to calculate the residual weight (%) (n = 3).

The *in vitro* biocompatibility of the microgels was investigated by coculturing the microgels and MC3T3 cells in a Transwell system and performing Live/Dead staining and the CCK-8 assay. For the Live/Dead staining, the MC3T3 cells were seeded into the lower Transwell chambers of a 12-well plate at a density of  $2 \times 10^4$ /well, whereas the microgels were placed in the upper chambers (pores of 0.4  $\mu\text{m}$ , Labselect). After 1, 2, and 3 days, the cells were stained with a Calcein/PI staining kit (C2015M, Beyotime) for 30 min, and the live cells in green and dead cells in red were observed under fluorescence microscopy. The numbers of live and dead cells were calculated using ImageJ software (n = 3). CCK-8 was used to quantitatively examine the proliferation of cells with microgels. The MC3T3 cells were seeded into the lower Transwell chambers (pores of 0.4  $\mu\text{m}$ , Labselect) of a 24-well plate at a density of  $2 \times 10^4$ /well, whereas the microgels were placed in the upper chambers. After 1, 2, and 3 days, the cells were incubated for 1 h with 10% CCK-8 solution (K009, ZETA Life) at 37 °C. The OD 450 value was recorded using a microplate reader (n = 3).

**In Vivo Degradation and Biocompatibility:** All animal experiments in this study were approved by the Animal Ethics Committee of West China Hospital, Sichuan University (Approval No. 20221114006). For *in vivo* degradation test, the microgels were implanted into the subcutaneous tissue of Sprague-Dawley rats (SD rats, male, 8 weeks old). On days 0, 1, 3, 5, and 7 after implantation, the skin tissues surrounding the implantation site were incised, and the microgels were observed and recorded using a digital camera. On day 7 after implantation, the rats were euthanized by inhalation of isoflurane. For *in vivo* biocompatibility assessment, the skin tissues surrounding the implantation site as well as major organs (heart, liver, spleen, lung, and kidney) of the rats were harvested and analyzed by HE staining (n = 3).

**Adhesion Capacity Test:** The *in vivo* adhesion capacity test of the microgels was conducted on the rat's abdominal wall, cecum, and tendon. The SD rats (male, 8 weeks old) were anesthetized by inhalation of isoflurane, and the target organ was exposed and separated. A wound was then made on the surface of the tissue to simulate damage in the surgical area. The microgels were then applied to the wound, and the surrounding tissue of the wound was then rubbed back and forth ten times using forceps. A digital camera was used to record this process. The number of microgels applied and the remaining ones were counted in the photograph, and the percentage of microgels remaining was calculated. All the experiments were performed in triplicate.

**In Vivo Hemostatic Ability:** For the liver hemorrhage and hemostasis model, the liver was separated and exposed through an abdominal midline incision after the SD rats (male, 8 weeks old) had been anesthetized. A preweighed piece of filter paper was placed beneath the liver. An incision with a diameter of 1.5 cm and a depth of 0.5 cm was made on the rat's liver using a scalpel. The microgels (100 mg) were immediately spread on the incision. When no obvious blood exudation was observed, the hemostatic time was recorded, and the total blood loss was calculated by the weight increment of the filter paper (n = 3). For the rat tail amputation hemorrhage and hemostasis model, the rat's tail was cut off with a length of 6 cm from the tip, and 100 mg of microgels were immediately spread on the incision. When no obvious blood exudation was observed, the hemostatic time was recorded, and the total blood loss was calculated (n = 3).

**In Vivo Prevention of Peritoneal Adhesion:** SD rats (male, 8 weeks old) were used for establishing the rat sidewall defect-cecum abrasion model to evaluate the efficacy of Janus-MGs for preventing peritoneal adhesion.<sup>[49]</sup> The rats were anesthetized by inhalation of isoflurane, and the cecum was exposed through an abdominal midline incision. The cecum was then gently abraded using a dry surgical gauze until spotted bleeding appeared. A 1.5  $\times$  2 cm defect was further made on the corresponding lateral abdominal wall, including the parietal peritoneum and partial muscle layer, using a scalpel. Subsequently, the surrounding mesentery was sutured to the normal abdominal wall to ensure contact between the abraded cecum and the defected abdominal wall. The microgels (500 mg) were applied to the surface of the injured abdominal wall and cecum. For the control group, 0.5 mL of sterile saline was applied to the injured tissue. On days 7 and 14

after surgery, the rats were euthanized, and the peritoneal adhesion was examined and scored using a standard adhesion scoring system (Table S2, Supporting Information).<sup>[68]</sup> The cecum and abdominal wall tissues related to the injury and adhesion were collected and analyzed by HE and Masson staining (n = 4).

**In Vivo Prevention of Intrauterine Adhesion:** According to a previous study,<sup>[69]</sup> the *in vivo* anti-adhesion effect of Janus-MGs was evaluated in a rat intrauterine adhesion model (SD rat, female, 8 weeks old). A self-matched grouping strategy was adopted for the model establishment and treatment: the left uteruses of all the rats were divided into the control group (n = 16); the right uteruses were equally divided into the sham group, HAMA-MGs group, DMA-MGs group, and Janus-MGs<sup>1/3</sup> group (n = 4). The uterus in the control group received a sterile saline application after experiencing a mechanical endometrial injury. The uterus in the sham group did not experience any injury. The uterus in the other groups received 100 mg of the corresponding microgel after experiencing injury. For the model establishment, the Y-shaped uteruses of the rats were exposed, and a 3 mm incision was made on the uterine horns. The endometrial injury was made by using a scraping spoon to repeatedly scratch the uterus through the incision. The uterus, abdominal wall, and skin were closed layer by layer. On days 7 and 14 after surgery, the uterus was collected and analyzed by HE and Masson staining. The endometrial thickness was determined by averaging four measurements taken at 90°, 180°, 270°, and 360° per horizontal cross-section using ImageJ software while concurrently quantifying the number of glands.

**In Vivo Prevention of Peritendinous Adhesion:** The rat peritendinous adhesion model was established by the adhesion formed between the tendon and the surrounding tissues during the repair process of an Achilles tendon injury. The model was established on both hindlimbs in 8-week-old male SD rats (n = 4). After anesthetization, the Achilles tendon was exposed and carefully separated. The tendon was then transected and sutured using the modified Kessler technique. Next, 200 mg of the corresponding microgels was applied to the injured tendon and the surrounding tissue for the treatment groups, whereas sterile saline was used in the control group. On days 14 and 21 after surgery, the repaired Achilles tendon was exposed, and the severity of peritendinous adhesion was quantified based on an adhesion scoring system (Table S3, Supporting Information).<sup>[70]</sup> The tendon tissue, along with the surrounding adhesion tissue, was then collected and analyzed by HE and Masson staining. A histological evaluation of the severity of peritendinous adhesion was performed based on previous reports (Table S4, Supporting Information).<sup>[71]</sup>

**Histological Staining:** All the harvested tissues were fixed in 4% paraformaldehyde for 48 h and then rinsed with DI water for 30 min. Subsequently, the tissues underwent dehydration, transparency treatment, and wax immersion in a dehydrator before being embedded in paraffin. Histological sections were then sliced continuously with a thickness of 4  $\mu\text{m}$ . Standard procedures involving HE and Masson staining were performed to show the histological structure of the tissues and possible adhesion. The paraffin sections were baked in an oven for 1 h at 65 °C. The sections were then immersed twice in xylene for 10 min and dehydrated in a gradient of ethanol. The sections were rinsed in running water for 3 min and then placed in DI water for 3 min. For the HE staining, the sections were stained with hematoxylin for 3 min, differentiated for 5 s, blued in a bluing solution for 1 min, and stained with eosin for 20 s. For the Masson staining, the sections were stained with freshly prepared Weigert's iron hematoxylin staining solution for 8 min, differentiated in an acidic ethanol differentiation solution for 10 s, blued in Masson's bluing solution for 5 min, stained with Biebrich scarlet-acid fuchsin staining solution for 10 min, washed in a molybdophosphoric acid solution for 2 min, stained with Aniline Blue staining solution for 2 min, and washed in a weak acid solution for 1 min. Finally, the sections were dehydrated in a gradient of ethanol, underwent transparency treatment in xylene, and then coverslipped using an automated coverslipper.

**Statistical Analysis:** All data were presented as mean  $\pm$  standard deviation. Statistical analysis was performed using GraphPad Prism (Version 9.5.0, GraphPad Software Inc., CA, USA). A one-way analysis of variance (ANOVA) was performed to assess the statistical significance among

multiple groups.  $p < 0.05$  indicates that the differences were statistically significant.

## Supporting Information

Supporting Information is available from the Wiley Online Library or from the author.

## Acknowledgements

Z.D. and Z.L. contributed equally to this work. This work was supported by the National Natural Science Foundation of China (82172394, 81873987, U22A20280, and 82302786), the National Key Research and Development Program of China (2022YFC2503100 and 2022YFC2503104), the 1.3.5 Project for Disciplines of Excellence, the West China Hospital, Sichuan University (2023HXFH012 and ZYGD23033), The China Postdoctoral Science Foundation (BX20230245 and 2023M742478), the Sichuan Science and Technology Program (2023YFH0068), and the Sichuan University Postdoctoral Interdisciplinary Innovation Fund (JCXK2226). The authors gratefully acknowledge Prof. Wei Qiang from the State Key Laboratory of Oral Diseases, the National Clinical Research Center for Oral Diseases, and the West China Hospital of Stomatology, Sichuan University, for his help in tribological tests.

## Conflict of Interest

The authors declare no conflict of interest.

## Data Availability Statement

The data that support the findings of this study are available from the corresponding author upon reasonable request.

## Keywords

Janus structure, microfluidic, microgel, postoperative adhesion

Received: May 9, 2024  
Revised: August 15, 2024  
Published online:

- [1] M. Trochsler, G. J. Maddern, *Lancet* **2014**, *383*, 8.
- [2] J. Liao, X. Li, Y. Fan, *Bioact. Mater.* **2023**, *26*, 387.
- [3] R. P. ten Broek, Y. Issa, E. J. van Santbrink, N. D. Bouvy, R. F. Kruitwagen, J. Jeekel, E. A. Bakkum, M. M. Rovers, H. van Goor, *BMJ* **2013**, *347*, f5588.
- [4] M. W. Healy, B. Schexnayder, M. T. Connell, N. Terry, A. H. DeCherney, J. M. Csokmay, B. J. Yauger, M. J. Hill, *Am. J. Obstet. Gynecol.* **2016**, *215*, 267.
- [5] T. Kuroiwa, P. C. Amadio, *Hand Clin.* **2023**, *39*, 171.
- [6] J. Zhou, H. Zhang, M. S. Fareed, Y. He, Y. Lu, C. Yang, Z. Wang, J. Su, P. Wang, W. Yan, K. Wang, *ACS Nano* **2022**, *16*, 7636.
- [7] J. Li, X. Feng, B. Liu, Y. Yu, L. Sun, T. Liu, Y. Wang, J. Ding, X. Chen, *Acta Biomater.* **2017**, *61*, 21.
- [8] R. P. G. Ten Broek, M. W. J. Stommel, C. Strik, C. van Laarhoven, F. Keus, H. van Goor, *Lancet* **2014**, *383*, 48.
- [9] W. Wu, R. Cheng, J. das Neves, J. Tang, J. Xiao, Q. Ni, X. Liu, G. Pan, D. Li, W. Cui, B. Sarmiento, *J. Controlled Release* **2017**, *261*, 48318.
- [10] Z. Li, L. Liu, Y. Chen, *Acta Biomater.* **2020**, *110*, 119.
- [11] M. Fujita, G. M. Policastro, A. Burdick, H. T. Lam, J. L. Ungerleider, R. L. Braden, D. Huang, K. G. Osborn, J. H. Omens, M. M. Madani, K. L. Christman, *Nat. Commun.* **2021**, *12*, 3764.
- [12] J. Chen, X. An, L. Xu, Y. Gao, M. Zhou, Z. Liu, *Small* **2024**, *20*, e2306598.
- [13] X. Liu, X. Song, Z. Zhang, S. Yang, L. Li, C. Lin, M. Chen, C. Liu, X. Li, Y. Zhang, G. Hu, *Adv. Sci.* **2023**, *10*, e2303767.
- [14] X. Wei, C. Cui, C. Fan, T. Wu, Y. Li, X. Zhang, K. Wang, Y. Pang, P. Yao, J. Yang, *Int. J. Biol. Macromol.* **2022**, *199*, 401.
- [15] Y. Jia, J. Feng, Z. Feng, J. Liu, Y. Yang, X. Li, M. Lei, H. Guo, Z. Wei, Y. Lv, F. Xu, *Proc. Natl. Acad. Sci. USA* **2023**, *120*, e2219024120.
- [16] K. Chen, C. Y. Liu, J. H. Huang, L. B. Che, Y. Yuan, C. S. Liu, *Adv. Funct. Mater.* **2023**, *33*, 2303836.
- [17] C. Hui, L. Q. Ding, T. C. Sun, Z. Liu, S. Ramakrishna, Y. Z. Long, J. Zhang, *Chem. Eng. J.* **2023**, *464*, 142458.
- [18] Y. Wang, L. R. Shang, G. P. Chen, L. Y. Sun, X. X. Zhang, Y. J. Zhao, *Sci. Adv.* **2020**, *6*, aax8258.
- [19] B. Kong, R. Liu, Y. Cheng, Y. Shang, D. Zhang, H. Gu, Y. Zhao, W. Xu, *Adv. Sci.* **2022**, *9*, e2203096.
- [20] Y. C. Lv, F. Y. Cai, X. K. Zhao, X. T. Zhu, F. A. Wei, Y. Q. Zheng, X. A. Shi, J. M. Yang, *Adv. Funct. Mater.* **2024**, *34*, 2314402.
- [21] J. Yu, Y. Qin, Y. Yang, X. Zhao, Z. Zhang, Q. Zhang, Y. Su, Y. Zhang, Y. Cheng, *Bioact. Mater.* **2023**, *19*, 703.
- [22] C. Y. Cui, T. L. Wu, X. Y. Chen, Y. Liu, Y. Li, Z. Y. Xu, C. C. Fan, W. G. Liu, *Adv. Funct. Mater.* **2020**, *30*, 202005689.
- [23] W. Peng, C. Liu, Y. Lai, Y. Wang, P. Liu, J. Shen, *Adv. Sci.* **2023**, *10*, e2301427.
- [24] H. Y. Feng, Y. F. Ma, Z. Z. Zhang, S. Yang, Z. F. Ma, Y. L. Zhang, S. H. Ma, B. Yu, M. R. Cai, X. W. Pei, F. Zhou, *Adv. Funct. Mater.* **2022**, *32*, 202111278.
- [25] G. S. Tang, R. H. Xiong, D. Lv, R. X. Xu, K. Braeckmans, C. B. Huang, S. C. De Smedt, *Adv. Sci.* **2019**, *6*, 201802342.
- [26] S. M. Mayes, J. Davis, J. Scott, V. Aguilar, S. A. Zawko, S. Swinnea, D. L. Peterson, J. G. Hardy, C. E. Schmidt, *Acta Biomater.* **2020**, *106*, 92.
- [27] J. H. Back, W. J. Cho, J. H. Kim, I. K. Park, S. W. Kwon, *Surg. Today* **2016**, *46*, 501.
- [28] S. Y. Na, S. H. Oh, K. S. Song, J. H. Lee, *Mater. Med.* **2012**, *23*, 2303.
- [29] A. A. Chaturvedi, O. R. Buayne, R. M. Lomme, T. Hendriks, H. Van Goor, *Surg. Infect.* **2015**, *16*, 410.
- [30] G. Chen, F. Wang, M. Nie, H. Zhang, H. Zhang, Y. Zhao, *PNAS* **2021**, *118*, e2112704118.
- [31] A. C. Daly, L. Riley, T. Segura, J. A. Burdick, *Nat. Rev. Mater.* **2020**, *5*, 20.
- [32] L. Yang, W. Yang, W. Xu, Y. Zhao, L. Shang, *Chem. Eng. J.* **2023**, *476*, 146797.
- [33] L. Xiang, J. Liang, Z. Wang, F. Lin, Y. Zhuang, Q. Saïding, F. Wang, L. Deng, W. Cui, *Sci. Adv.* **2023**, *9*, ead9375.
- [34] K. M. Usher, S. Zhu, G. Mavropalias, J. A. Carrino, J. Zhao, J. Xu, *Bone Res.* **2019**, *7*, 9.
- [35] C. Cao, F. Wu, X. Niu, X. Hu, J. Cheng, Y. Zhang, C. Li, X. Duan, X. Fu, J. Zhang, X. Zhang, Y. Ao, *Theranostics* **2020**, *10*, 10573.
- [36] J. Zhang, C. Xiao, X. Zhang, Y. Lin, H. Yang, Y. S. Zhang, J. Ding, *J. Controlled Release* **2021**, *335*, 359.
- [37] Y. Cai, F. Wu, Y. Yu, Y. Liu, C. Shao, H. Gu, M. Li, Y. Zhao, *Acta Biomater.* **2019**, *84*, 222.
- [38] G. S. Tang, L. Chen, L. M. Lian, F. H. Li, H. Ravanbakhsh, M. A. Wang, Y. S. Zhang, C. B. Huang, *Chem. Eng. J.* **2021**, *407*, 127187.
- [39] C. Hong, B. D. Olsen, P. T. Hammond, *Biomaterials* **2022**, *283*, 121432.
- [40] Y. Guo, Y. Wang, X. Zhao, X. Li, Q. Wang, W. Zhong, K. Mequanint, R. Zhan, M. Xing, G. Luo, *Sci. Adv.* **2021**, *7*, abf9635.
- [41] J. Yang, F. Cai, Y. Lv, T. Jiang, X. Zhao, X. Hu, Y. Zheng, X. Shi, *Int. J. Biol. Macromol.* **2024**, *257*, 128561.

- [42] J. Li, W. Cao, X. X. Lv, L. Jiang, Y. J. Li, W. Z. Li, S. Z. Chen, X. Y. Li, *Acta Pharmacol. Sin.* **2013**, *34*, 367.
- [43] H. Li, X. Zhou, L. Luo, Q. Ding, S. Tang, *Carbohydr. Polym.* **2022**, *281*, 119039.
- [44] G. Wang, X. Meng, P. Wang, X. Wang, G. Liu, D. A. Wang, C. Fan, *Biomaterials* **2022**, *291*, 121908.
- [45] Y. Mi, F. Yang, C. Bloomquist, Y. Xia, B. Sun, Y. Qi, K. Wagner, S. A. Montgomery, T. Zhang, A. Z. Wang, *Adv. Sci.* **2019**, *6*, 1900809.
- [46] J. Yu, K. Wang, C. Fan, X. Zhao, J. Gao, W. Jing, X. Zhang, J. Li, Y. Li, J. Yang, W. Liu, *Adv. Mater.* **2021**, *33*, 2008395.
- [47] X. Song, Z. Zhang, Z. Shen, J. Zheng, X. Liu, Y. Ni, J. Quan, X. Li, G. Hu, Y. Zhang, *ACS Appl. Mater. Interfaces* **2021**, *13*, 56881.
- [48] C. H. Chen, S. H. Chen, S. H. Mao, M. J. Tsai, P. Y. Chou, C. H. Liao, J. P. Chen, *Carbohydr. Polym.* **2017**, *173*, 721.
- [49] E. S. Zhang, J. H. Yang, K. Wang, B. Y. Song, H. Zhu, X. F. Han, Y. J. Shi, C. B. Yang, Z. P. Zeng, Z. Q. Cao, *Adv. Funct. Mater.* **2021**, *31*, 2009431.
- [50] I. Kusuki, I. Suganuma, F. Ito, M. Akiyama, A. Sasaki, K. Yamanaka, H. Tatsumi, J. Kitawaki, *Surg. Laparosc. Endosc. Percutan. Tech.* **2014**, *24*, e13.
- [51] C.-H. Chen, S.-H. Chen, S.-H. Mao, M.-J. Tsai, P.-Y. Chou, C.-H. Liao, J.-P. Chen, *Carbohydr. Polym.* **2017**, *173*, 721.
- [52] E. Y. Sikar, H. E. Sikar, H. Top, A. C. Aycit, *TJTES* **2019**, *25*, 93.
- [53] Y. T. Song, L. Dong, J. G. Hu, P. C. Liu, Y. L. Jiang, L. Zhou, M. Wang, J. Tan, Y. X. Li, Q. Y. Zhang, C. Y. Zou, X. Z. Zhang, L. M. Zhao, R. Nie, Y. Zhang, J. Li-Ling, H. Q. Xie, *Compos. Part B: Eng.* **2023**, *250*, 110461.
- [54] X. X. Zhang, G. P. Chen, Y. T. Wang, L. Fan, Y. J. Zhao, *Adv. Sci.* **2022**, *9*, 2104883.
- [55] B. F. Xu, M. J. Zhou, M. Y. Liu, Z. Wang, J. R. Duan, W. Z. Li, W. G. Cui, A. J. Zhang, *Small* **2023**, *19*, 2300481.
- [56] L. Xin, C. Wei, X. Tong, Y. Dai, D. Huang, J. Chen, L. Ma, S. Zhang, *Bioact. Mater.* **2022**, *12*, 107.
- [57] L. Feng, L. Wang, Y. Ma, W. Duan, S. Martin-Saldaña, Y. Zhu, X. Zhang, B. Zhu, C. Li, S. Hu, M. Bao, T. Wang, Y. Zhu, F. Yang, Y. Bu, *Bioact. Mater.* **2023**, *27*, 82.
- [58] W. Xia, Q. Wang, M. Liu, S. Lu, H. Yu, H. Yin, M. You, Q. Chen, B. Wang, F. Lin, *ACS Appl. Mater. Interfaces* **2023**, *15*, 44676.
- [59] J. Sun, F. Ju, J. Jin, H. L. Wang, Z. J. Li, Y. C. Sun, Q. Z. Chen, Q. Q. Yang, J. Tan, Y. L. Zhou, *Small* **2023**, *19*, 2300326.
- [60] R. Dang, L. Chen, F. Sefat, X. Li, S. Liu, X. Yuan, X. Ning, Y. S. Zhang, P. Ji, X. Zhang, *Small* **2022**, *18*, e2105255.
- [61] B. R. Freedman, A. Kuttler, N. Beckmann, S. Nam, D. Kent, M. Schuleit, F. Ramazani, N. Accart, A. Rock, J. Y. Li, M. Kurz, A. Fisch, T. Ullrich, M. W. Hast, Y. Tinguely, E. Weber, D. J. Mooney, *Nat. Biomed. Eng.* **2022**, *6*, 1167.
- [62] C. Cai, X. Zhang, Y. Li, X. Liu, S. Wang, M. Lu, X. Yan, L. Deng, S. Liu, F. Wang, C. Fan, *Adv. Mater.* **2022**, *34*, 2106564.
- [63] Z. Wang, L. Xiang, F. Lin, Y. Tang, L. Deng, W. Cui, *Adv. Mater.* **2022**, *34*, 2200789.
- [64] G. M. Bürgisser, J. Buschmann, *J. Biomed. Mater. Res. Part B Appl. Biomater.* **2015**, *103*, 212.
- [65] D. Wei, W. Xiao, J. Sun, M. Zhong, L. Guo, H. Fan, X. Zhang, *J. Mater. Chem. B.* **2015**, *3*, 2753.
- [66] M. Wang, W. Li, J. Hao, A. Gonzales III, Z. Zhao, R. S. Flores, X. Kuang, X. Mu, T. Ching, G. Tang, Z. Luo, C. E. Garciamendez-Mijares, J. K. Sahoo, M. F. Wells, G. Niu, P. Agrawal, A. Quiñones-Hinojosa, K. Eggen, Y. S. Zhang, *Nat. Commun.* **2022**, *13*, 3317.
- [67] Y. Lei, Y. Wang, J. Shen, Z. Cai, C. Zhao, H. Chen, X. Luo, N. Hu, W. Cui, W. Huang, *Sci. Adv.* **2022**, *8*, eabl6449.
- [68] R. Mizuta, Y. Mizuno, X. Chen, Y. Kurihara, T. Taguchi, *Acta Biomater.* **2021**, *121*, 328.
- [69] C. Dong, C. Yang, M. R. Younis, J. Zhang, G. He, X. Qiu, L. H. Fu, D. Y. Zhang, H. Wang, W. Hong, J. Lin, X. Wu, P. Huang, *Adv. Sci.* **2022**, *9*, e2102220.
- [70] X. Rong, Y. Tang, S. Cao, S. Xiao, H. Wang, B. Zhu, S. Huang, M. Adeli, R. D. Rodriguez, C. Cheng, L. Ma, L. Qiu, *ACS Nano* **2023**, *17*, 16501.
- [71] C. Cai, X. Zhang, Y. Li, X. Liu, S. Wang, M. Lu, X. Yan, L. Deng, S. Liu, F. Wang, C. Fan, *Adv. Mater.* **2022**, *34*, 2106564.